



# **Origin of the shallow slip deficit on a strike slip fault: Influence of elastic structure, topography, data coverage, and noise**

Mathilde Marchandon, James Hollingsworth, Mathilde Radiguet

## **► To cite this version:**

Mathilde Marchandon, James Hollingsworth, Mathilde Radiguet. Origin of the shallow slip deficit on a strike slip fault: Influence of elastic structure, topography, data coverage, and noise. *Earth and Planetary Science Letters*, 2021, 554, pp.116696. <10.1016/j.epsl.2020.116696>. <hal-03454847>

**HAL Id: hal-03454847**

**<https://hal.science/hal-03454847v1>**

Submitted on 15 Dec 2022

**HAL** is a multi-disciplinary open access archive for the deposit and dissemination of scientific research documents, whether they are published or not. The documents may come from teaching and research institutions in France or abroad, or from public or private research centers.

L'archive ouverte pluridisciplinaire **HAL**, est destinée au dépôt et à la diffusion de documents scientifiques de niveau recherche, publiés ou non, émanant des établissements d'enseignement et de recherche français ou étrangers, des laboratoires publics ou privés.



Distributed under a Creative Commons CC BY-NC 4.0 - Attribution - Non-commercial use - International License

# Origin of the Shallow Slip Deficit on a strike slip fault: influence of elastic structure, topography, data coverage, and noise

Mathilde Marchandon<sup>a,\*</sup>, James Hollingsworth<sup>a</sup>, Mathilde Radiguet<sup>a</sup>

<sup>a</sup>*Univ. Grenoble Alpes, Univ. Savoie Mont Blanc, CNRS, IRD, IFSTTAR, ISTerre,  
38000 Grenoble, France*

---

## Abstract

Numerous fault slip models for several large strike-slip earthquakes indicate a reduction of slip along the uppermost part of the fault (Shallow Slip Deficit, SSD). In this paper, we investigate the possibility that the SSD is an artifact due to the simplifications made when we model the medium. Using a set of synthetic data for the 1992 Landers earthquake, we show that while neglecting the topography of the Landers area has a moderate impact on the retrieved slip model, neglecting variations in elastic properties, in particular the variation with depth, leads to significant bias on the slip model and can produce 25% of artifact (a smaller impact). We further show that a lack of data coverage around the fault further increases the amount of artificial SSD. Moreover, we find that correlated data noise with maximum amplitude as low as 5% of the maximum surface displacement can also produce significant artificial SSD. We conclude

---

\*Corresponding author  
*Email address:*  
Marchandon)

that simple elastic forward modelling in a homogeneous medium may be inappropriate for resolving slip-variability with depth, even in areas of limited topography or lateral variation in elastic properties. Finally, we argue that the estimation of model uncertainty due to data error should be systematic in inversion studies to avoid any misinterpretation of the slip distribution.

*Keywords:* Strike-slip earthquake, Shallow Slip Deficit, Fault slip inversion, Pylith, Topography, Elastic properties

---

## 1. Introduction

Fault slip models inferred from geodetic data (InSAR and GPS) for several large (Mw7+) continental strike-slip earthquakes indicate a reduction of slip near the surface, along the uppermost part of the fault. Slip is typically at a maximum between 3 and 6 km, decreasing both down-dip and up-dip towards the surface (i.e. Fialko et al., 2005; Dolan & Haravitch, 2014). Averaged over many seismic cycles, slip on crustal-scale strike-slip faults should be uniform with depth (Reid, 1910; Tse & Rice, 1986). Several hypotheses have thus been proposed to account for this Shallow Slip Deficit (SSD). One simple explanation is that the slip deficit is accommodated at some other time during the seismic cycle by smaller earthquakes. Very shallow surface rupturing earthquakes would thus be needed to relieve the remaining elastic stresses. However, given the slip deficit is generally confined to depths  $< 5$  km, where earthquakes cannot easily nucleate due to the low crustal stresses, such events are unlikely to relieve SSD. An alternative explanation is that SSD is accommodated aseismically by postseismic or interseismic shallow creep. However, interseismic shallow creep has only been observed for a relatively

18 small number of faults (e.g. Lindsey et al., 2014; Rousset et al., 2016), while  
 19 shallow afterslip is typically too small to compensate for the slip deficit (e.g.  
 20 Fialko, 2004a). Another explanation is that a part of the coseismic strain in  
 21 the uppermost crust is accommodated through inelastic deformation in the  
 22 volume surrounding the fault (Simons et al., 2002; Fialko et al., 2005; Kaneko  
 23 & Fialko, 2011). Dynamic rupture simulations incorporating off-fault plastic  
 24 yielding indicate that off-fault inelastic deformation can account for up to  
 25 15% of SSD (Kaneko & Fialko, 2011). However, this amount is substan-  
 26 tially less than the 45% SSD that has been observed for some earthquakes  
 27 (Fialko et al., 2005). Finally, SSD, or at least a part of it, may result from  
 28 modeling artifacts. Kaneko & Fialko (2011) showed that inverting synthetic  
 29 surface displacements produced in an elasto-plastic medium using a purely  
 30 elastic forward model can produce up to 11% artificial SSD. Furthermore,  
 31 Xu et al. (2016) showed that a significant part of the apparent SSD inferred  
 32 from geodetic inversions could be an artifact resulting from a lack of data  
 33 coverage close to the surface rupture. Indeed, data sparsity close to the fault  
 34 reduces the resolution of the shallow part of the model.

35 Understanding the origin of SSD, and more generally, understanding how  
 36 the deformation is distributed and accommodated within upper crustal fault  
 37 zones is fundamental for correct seismic hazard estimation. If SSD is real,  
 38 then fault slip rates deduced from offset geological markers could be signifi-  
 39 cantly underestimated if the distributed off-fault deformation component is  
 40 not captured in the offset measurement. Consequently, the estimation of  
 41 seismic hazard using probabilistic approaches incorporating geological fault  
 42 slip rates could lead to a systematic underestimation of the real hazard.

43 In this paper, we explore whether SSD could be an artifact due to the  
44 simplifications made when we model the fault slip. At present, the use of  
45 homogeneous half-space models based on analytical solutions developed by  
46 Okada (1992) are ubiquitous when inferring the distribution of slip on the  
47 fault during an earthquake (e.g. Jonsson et al., 2002; Xu et al., 2016; Hamling  
48 et al., 2017; Ross et al., 2019). As a first order improvement of the homo-  
49 geneous half-space models, some studies use stratified models that take into  
50 account the increase of the shear modulus with depth. Although using ho-  
51 mogeneous half-space and 1D layered models is a fast and easy way to study  
52 seismic sources, it provides only a first approximation of the real structure of  
53 the crust, neglecting the surface topography and the 3D variation in elastic  
54 properties. Recent studies focusing on subduction zones show that neglecting  
55 these effects can significantly bias fault slip models (e.g. Williams & Wallace,  
56 2015, 2018; Langer et al., 2019). In this paper we explore whether the same  
57 is true for a strike-slip fault in a continental setting, where variations in elas-  
58 tic structure and topography are more limited, and near-field data is more  
59 readily available.

60 Focusing on the 1992 Mw 7.3 Landers earthquake, we evaluate, through a  
61 set of forward models and synthetic inversions, how the simplifications made  
62 when we model the medium can alter the inferred slip distribution and, in  
63 particular, the amount of slip at shallow depths. We select the 1992 Mw  
64 7.3 Landers earthquake for two reasons. First, the most recent estimation  
65 of the SSD for this earthquake, inferred from a very complete set of surface  
66 displacements (incorporating optical correlation, InSAR, GPS, and triangu-  
67 lation data), is 41% (Gombert et al., 2017), while the amount of shallow

68 afterslip observed for this earthquake ( $<20$  cm) is not sufficient to account  
 69 for this deficit (Fialko, 2004a). This shows that the origin of SSD for this  
 70 earthquake is not fully understood and thus merits further investigation.  
 71 Secondly, a 3D high resolution velocity model is available for the Landers  
 72 region, thereby allowing us to precisely estimate the 3D variations in elastic  
 73 properties throughout the medium (Share et al., 2019). Using the finite ele-  
 74 ment code PyLith (Aagaard et al., 2013), we first show, via forward modeling  
 75 with a prescribed slip distribution for the Landers earthquake, that topogra-  
 76 phy and variation in elastic properties can change the surface displacement  
 77 field significantly. Then, inverting these synthetic surface displacements, we  
 78 show that neglecting the medium complexity can significantly alter the re-  
 79 sulting slip distribution and produce artificial SSD. Finally, we explore how  
 80 the distribution of surface data (i.e. data gaps near the fault, quadtree data  
 81 discretization) and correlated data noise can impact our results.

## 82 **2. Impact of medium complexities on the surface displacements** 83 **and fault slip model**

### 84 *2.1. Impact of medium complexities on the surface displacements*

To evaluate the impact of the topography and the 3D variation in elastic  
 properties on the surface displacements of the Landers earthquake, we use  
 the finite element code PyLith (Aagaard et al., 2013). Using the fault slip  
 model of Hernandez et al. (1999) for the Landers earthquake (Figure 2a), we  
 compare the surface displacement field computed in three different mediums:  
 (1) a medium with uniform elastic properties and a flat surface (**homo-  
 flat model**); (2) a medium with uniform elastic properties and topography

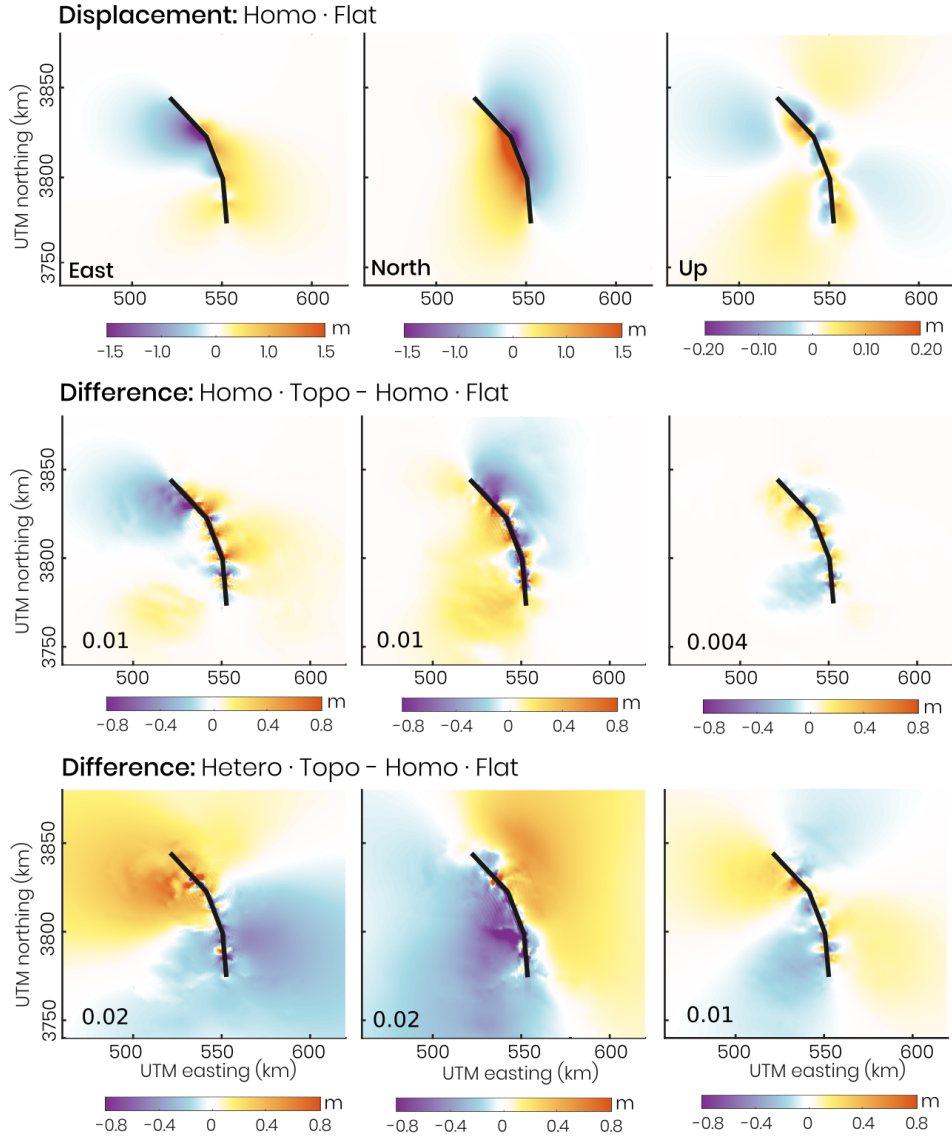


Figure 1: Effect of the medium complexities on the surface displacements. First row: Synthetic surface displacement field for the Landers earthquake computed in a homogeneous and flat medium (homo-flat model). Second row: Difference between the synthetic surface displacement field computed in a homogeneous medium with topography (homo-topo model) and the homo-flat model. Third row: Difference between the synthetic surface displacement field computed in a heterogeneous medium with topography (hetero-topo model) and the homo-flat model. The RMS of the differences is indicated on each subplot (in meters). The slip model used to compute the surface displacements is from Hernandez et al. (1999), the topography is from the ASTER GDEM downsampled at 5 km and the 3D elastic properties used for the heterogeneous model are estimated from the velocity model of Share et al. (2019).

(**homo-topo model**); and (3) a medium with 3D variations in elastic properties and topography (**hetero-topo model**). The synthetic displacements for the three different forward models are thus:

$$\mathbf{d}_{HoF} = \mathbf{G}_{HoF} \mathbf{m}_{Her} \quad (1)$$

$$\mathbf{d}_{HoTo} = \mathbf{G}_{HoTo} \mathbf{m}_{Her} \quad (2)$$

$$\mathbf{d}_{HeTo} = \mathbf{G}_{HeTo} \mathbf{m}_{Her} \quad (3)$$

85 where  $\mathbf{d}_{HoF}$ ,  $\mathbf{d}_{HoTo}$ , and  $\mathbf{d}_{HeTo}$  are the synthetic data computed in the  
 86 homogeneous and flat medium, the homogeneous medium with topography,  
 87 and the heterogeneous medium with topography respectively;  $\mathbf{G}_{HoF}$ ,  $\mathbf{G}_{HoTo}$ ,  
 88 and  $\mathbf{G}_{HeTo}$  are the Green's functions computed in the homogeneous and flat  
 89 medium, the homogeneous medium with topography, and the heterogeneous  
 90 medium with topography respectively; and  $\mathbf{m}_{Her}$  is the distributed slip model  
 91 of Hernandez et al. (1999).

92 We choose the fault slip distribution of Hernandez et al. (1999) as our  
 93 input slip model for this synthetic study because the fault geometry of this  
 94 model is simple (composed of 3 segments) and thus easy to model. The mesh  
 95 of the finite element model is constructed with the Trelis software. For each  
 96 case, the dimension of the finite element model is 1,200 km x 600 km x 600  
 97 km along east, north, and vertical directions, respectively, and contains  $\sim 1$   
 98 million tetrahedra cells. To reduce the computation time, while keeping ac-  
 99 curate results near the fault, the cell size is 2 km on and within 100 km of the  
 100 fault, gradually decreasing to 20 km toward the edges of the model. We use  
 101 the ASTER GDEM downsampled at 5 km to model the surface topography.  
 102 For the homogeneous mediums (models 1 and 2), we assume a Poisson ratio

103 of 0.26. For the heterogeneous medium, we derive the 3D elastic properties  
 104 using the new 3D Southern California velocity model of Share et al. (2019),  
 105 applying the empirical relationship of Brocher (2005) to estimate the density  
 106 from P-wave velocities. Although the elastic properties of our model vary  
 107 in the three directions, in the area of interest, the variation with depth is  
 108 significantly greater than the horizontal plane. A cross-section and various  
 109 profiles showing the depth and lateral variations of the shear modulus are  
 110 shown in Figure S1. To evaluate the accuracy of our finite element model,  
 111 the surface displacements of the homo-flat model are compared with those  
 112 computed using the analytic solution of Okada (Figure S2). The differences  
 113 are very small ( $\sim 1.5\%$  over distances of  $\sim 10$  km from the fault) and mainly  
 114 due to differences in the fault discretization between the FEM and Okada  
 115 models. Results of the comparison between the surface displacements pro-  
 116 duced by the homo-flat, homo-topo, and hetero-topo models are shown in  
 117 Figure 1. When the topography is taken into account, differences with the  
 118 homogeneous and flat model are up to 6 cm (Figure 1, second row) and are  
 119 localized within  $\sim 30$  km of the fault. When both the topography and the  
 120 heterogeneous elastic properties are considered, significant differences with  
 121 maximum amplitudes of 15 cm are visible across the entire region (Figure  
 122 1, third row). On the north-south component, the differences show that the  
 123 amplitude of the displacements of the hetero-topo model are lower than those  
 124 of the homo-flat model.

125 *2.2. Impact of neglecting the complexities of the medium on the inferred fault*  
 126 *slip model*

127 To evaluate the impact of neglecting the complexities of the medium on  
 128 the inferred slip model, we invert the synthetic surface displacement field  
 129 computed in the non-flat and heterogeneous mediums using Green’s func-  
 130 tions calculated in the homogeneous and flat medium. In doing so, we aim  
 131 at reproducing a typical slip inversion scenario in which real coseismic dis-  
 132 placements are inverted assuming a simplified representation of the crust (i.e.  
 133 elastic half-space). The objective is to evaluate the error made on the in-  
 134 ferred fault slip model. We perform three inversions, one for each synthetic  
 135 data set computed in the previous section. The slip on the fault is retrieved  
 136 using a constrained least square inversion (Coleman & Li, 1992) and a Lapla-  
 137 cian smoothing operator is implemented to reduce the slip variations between  
 138 neighboring patches. For each inversion, we constrain the slip between 0 and  
 139 15 m, and we fix the rake to 180°. We thus resolve the following system of  
 140 equations:

$$\begin{bmatrix} \mathbf{d} \\ 0 \end{bmatrix} = \begin{bmatrix} \mathbf{G}_{HoF} \\ \lambda \mathbf{D} \end{bmatrix} \mathbf{m} \quad (4)$$

141 where  $\mathbf{d}$  is the synthetic data vector computed in one of three tested  
 142 mediums (i.e.  $\mathbf{d}_{HoF}$ ,  $\mathbf{d}_{HoTo}$ , or  $\mathbf{d}_{HeTo}$ ),  $\mathbf{G}_{HoF}$  is the Green’s function matrix  
 143 relating the surface displacements to the slip model in the homogeneous and  
 144 flat medium,  $\mathbf{m}$  the vector of parameters we are solving for (right-lateral slip  
 145 on each sub-fault),  $\mathbf{D}$  the second-order finite difference operator, and  $\lambda$  the  
 146 smoothing factor. We set  $\lambda$  according to an L-curve criterion (Figure S3)  
 147 and use the same value for the three inversions.

Figure 2 shows the resulting slip models for the three inversions, along with their moment magnitude, and residual displacement (relative to the input slip model). When the homo-flat synthetic data are inverted, the input slip model is very well retrieved (Figure 2b), given the same Green’s function matrix is used in both the forward and inverse model. The only noticeable difference is that the retrieved slip model is slightly smoother than the input slip model. When the homo-topo data are inverted, the input slip model is quite well retrieved, although there are some significant differences at depths of 10-15 km (average difference: +0.70 m). Indeed, slip in the homo-topo model extends deeper in the crust than in the input slip model (Figure 2c). This leads to a slightly higher moment magnitude for this model. Finally, when the hetero-topo data are inverted, the slip is well retrieved between 0–3 km, largely overestimated between 3–6 km (average difference: +0.74 m), and underestimated between 6–15 km (average difference: -0.82 m, Figure 2d). The moment magnitude is slightly lower than in the input slip model.

The distributions of normalized cumulative slip with depth for the input slip model and for the three retrieved slip models are shown in Figure 3. As the amount of SSD is dependent on the smoothing applied (e.g. Gombert et al., 2017; Huang et al., 2017; Li et al., 2020), we also plot the distribution of normalized cumulative slip with depth for the range of models located in the “corner” of the L-curve (shaded area around the solid line in Figure 3 and Figure S3). This allows us to estimate the SSD uncertainty due to the smoothing. The SSD of the homo-flat model is higher than the SSD of the input slip model ( $16\pm0.8\%$  versus  $10\%$ , respectively), while the SSD of the homo-topo model is slightly lower ( $8\pm0.6\%$ ). It is also worth noting

173 that the profiles of cumulative slip with depth for the input and homo-flat  
 174 slip models look quite different, particularly at depth, due to the smoothing  
 175 applied. For the hetero-topo model, the difference is much more significant,  
 176 with a SSD of  $35 \pm 4\%$ ,  $\sim 3.5$  times larger than the SSD of the input slip  
 177 model. Given this large increase only occurs in the hetero-topo model, this  
 178 artificial SSD must result from neglecting the variations in elastic properties  
 179 when we computed the Green's functions. To confirm this, we also perform  
 180 the hetero-flat inversion (i.e. inversion of the synthetic data computed in a  
 181 heterogeneous and flat medium) and find that the slip distribution and the  
 182 amount of artificial SSD of the hetero-flat and hetero-topo models are very  
 183 similar (Figure S4).

184 Surface displacement residuals for the three retrieved slip models (model  
 185 predictions minus data) are shown in Figure S5. Predictions of the homo-flat  
 186 model are very good (i.e. very low RMS of  $3 \times 10^{-4}$  m), which is expected  
 187 given both the forward and inverse model used the same medium. However,  
 188 the homo-topo and hetero-topo models both show larger residuals. For the  
 189 homo-topo model the residuals are relatively low (RMS of  $2.3 \times 10^{-3}$  m),  
 190 and are located near the fault (within  $\sim 20$  km). On the contrary, residuals  
 191 for the hetero-topo model are relatively high (RMS of  $8.3 \times 10^{-3}$  m) and are  
 192 present in both the near- and far-field. The spatial pattern of residuals for  
 193 each component is anti-symmetrical with respect to the fault.

### 194 **3. Impact of the surface data distribution on the amount of SSD**

195 Data used in fault slip inversions are often unevenly distributed. For ex-  
 196 ample, for major earthquakes, InSAR data suffers from decorrelation near the

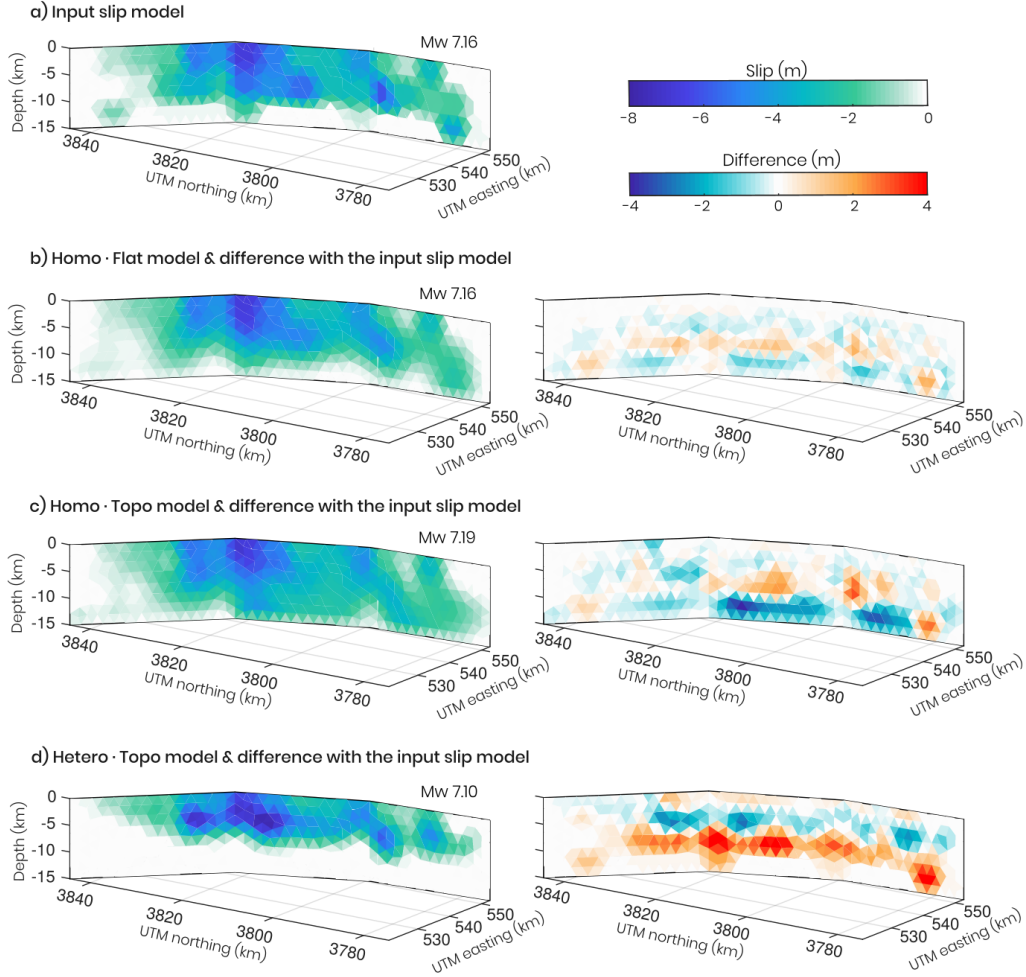


Figure 2: Effect of neglecting the medium complexities on the retrieved slip models. (a) Input slip model for the Landers earthquake (from Hernandez et al. (1999)). (b-d) Left side: Retrieved slip models obtained from the inversion of the synthetic data computed in a homogeneous and flat medium (homo-flat model), homogeneous medium with topography (homo-topo model), and heterogeneous medium with topography (hetero-topo model). Right side: Difference between the retrieved slip models and the input slip model. The moment magnitude is indicated next to each model. All slip models have been obtained using Green's functions computed assuming a homogeneous and flat medium.

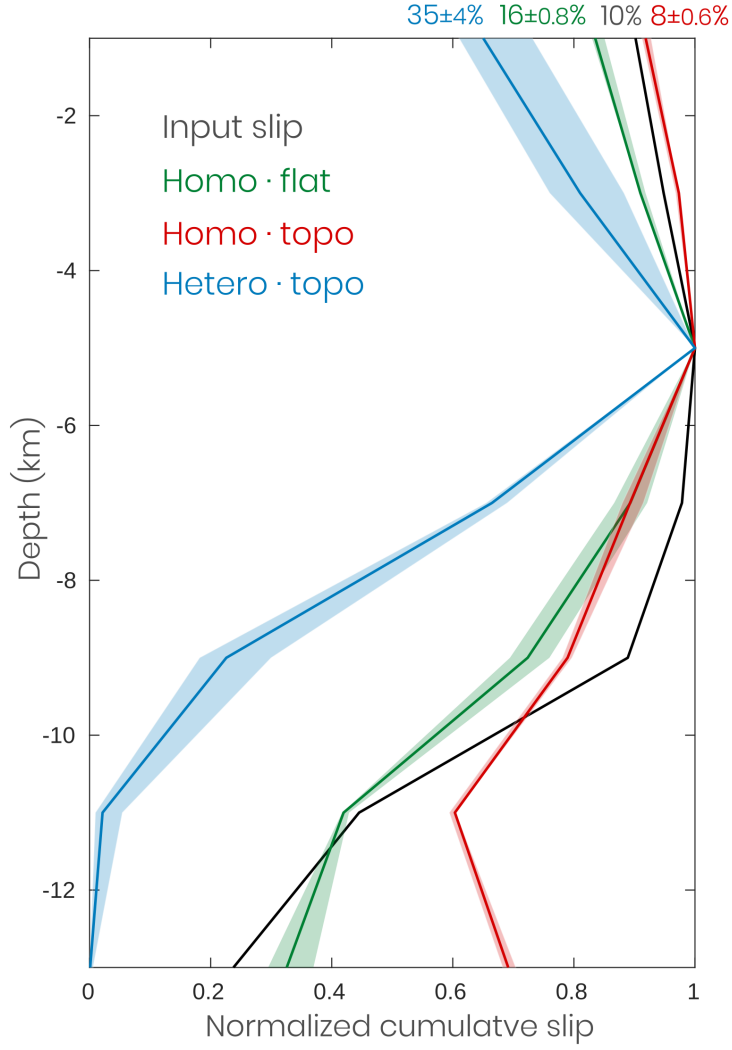


Figure 3: Normalized cumulative slip with depth of the input slip model and the three retrieved slip models. The shaded area of each curve represents the uncertainty due to the smoothing of the distribution of cumulative slip with depth. The amount of SSD is indicated at the top of each curve.

197 fault, where displacement gradients are high. If no other data are available,  
198 this leads to an incomplete description of the surface displacements close to  
199 the fault. Xu et al. (2016) argued that the lack of data coverage close to the  
200 surface rupture is responsible for a significant part of the SSD inferred by  
201 geodetic inversions. By reassessing the slip model of three  $M_w > 7$  strike-slip  
202 earthquakes using near-fault data, in addition to previously used GPS and  
203 InSAR data, they showed that adding near-field data decreases the inferred  
204 SSD by  $\sim 30\%$ . Furthermore, to reduce computation time, high-resolution  
205 data are often discretized using a quadtree algorithm (e.g. Jonsson et al.,  
206 2002). This algorithm keeps high spatial sampling in areas where the dis-  
207 placement gradients are high (i.e. near the fault for strike-slip earthquakes)  
208 and downsamples data in areas where the displacement gradient is low. By  
209 increasing the number of points near the fault, a quadtree decomposition  
210 gives higher weight to near-fault data used in the inversion, while decreas-  
211 ing the weight of far-field data. Such a difference in the data distribution  
212 may also impact the inferred fault slip, especially if the shallow elastic struc-  
213 ture (and topography) differ substantially from the homogeneous-flat case  
214 (i.e. erroneous Green's functions in the shallow crust may be weighted more  
215 strongly in the inversion).

216 In this section, we evaluate the impact of the surface data distribution on  
217 the amount of artificial SSD inferred from the hetero-topo inversion experi-  
218 ment (i.e. Section 3). We first evaluate the impact of data gaps around the  
219 fault having different sizes (5, 10, and 15 km, Figure S6). Then, we evaluate  
220 the impact of a quadtree distribution compared to a uniform data distribu-  
221 tion (Figure S6). The retrieved slip models of the data gap and quadtree

222 tests are shown in Figure 4 and S7, while the distribution of cumulative slip  
223 with depth are shown in Figure 4. The residuals between data and model  
224 predictions for each model are shown in Figure S8.

225 As the data gap increases close to the fault, the resulting slip decreases  
226 between 0 and 2 km (mean slip of  $\sim 2$ , 1.6, and 1.3 m for a data gap of 5, 10,  
227 and 15 km), and increases between 2 and 6 km (mean slip of  $\sim 3.1$ , 3.8, and  
228 3.9 m for a data gap of 5, 10, and 15 km). Consequently, the shallow slip  
229 deficit increases with the width of the data gap (Figure 4, SSD of  $45 \pm 6\%$ ,  
230  $60 \pm 9\%$  and,  $68 \pm 11\%$  for a data gap of 5, 10, and 15 km, respectively). The  
231 shallow slip being less constrained when there is not data close to the fault,  
232 the SSD uncertainty increases with the width of the data gap (Figure S9).  
233 The main differences between the slip model obtained with evenly distributed  
234 data versus the one obtained using a quadtree distribution is that slip ex-  
235 tends deeper in the latter case, while the amplitude at mid-depths is also  
236 lower (Figure 4,  $\sim 2.8$  m), thereby leading to a reduction in SSD (Figure 4,  
237  $25 \pm 1.5\%$ ). Finally, when the surface data have a quadtree distribution and  
238 a data gap of 10 km width close to the fault, the inferred SSD is  $44 \pm 2.8\%$   
239 (Figure 4).

240 To evaluate if the impact of the data distribution is identical when the  
241 medium is well represented by the Green's functions, we perform the same  
242 test for the homo-flat case. We find that the retrieved slip models are very  
243 similar whatever the surface data distribution (Figure S10). Concerning  
244 the amount of SSD, we observe the same general tendency; i.e. the SSD  
245 increases when there is a data gap close to the fault and decreases when  
246 the data has a quadtree distribution, albeit at a significantly lower extent

247 (SSD of 16%, 19% and 13.5% for the uniform, 10 km data gap, and quadtree  
248 distribution respectively, Figure S11). Indeed, for the homo-flat case, the  
249 Green's functions used to compute the synthetic data are identical to the  
250 Green's functions used in the inversion; the model that best fits the data is  
251 therefore very similar regardless of the surface data distribution.

#### 252 **4. Impact of correlated noise on the amount of SSD**

253 InSAR and optical data used in inversion studies exhibit correlated data  
254 errors that arise from a multitude of sources (e.g. phase propagation delays  
255 through the atmosphere for InSAR data or difference in shadowing between  
256 pre- and post-images for optical data). This noise can be partially fit by  
257 the inversion and therefore can bias the inferred slip model. To evaluate  
258 the impact of noise on our results, we add synthetic correlated noise with  
259 correlation length  $L_c$  and maximum amplitude  $A_{max}$  to the synthetic data.  
260 We test correlation length values of 2 km, 5 km, and 10 km and maximum  
261 amplitude values of 1 cm (low noise), 5 cm (medium noise), and 10 cm  
262 (high noise) corresponding to 0.4%, 2%, and 4% of the maximum surface  
263 displacement. For each noise characteristic (correlation length and maximum  
264 amplitude), 300 simulations of noise are generated (Figure S12). Each noise  
265 simulation is then added to the original synthetic data and the 300 new  
266 datasets are inverted using the Green's functions computed in a homogeneous  
267 and flat medium. We test the impact of noise on the homo-flat and hetero-  
268 topo inversions and for the various data distributions tested previously (i.e.  
269 uniform data distribution, near-fault data gap of 10 km width, quadtree  
270 distribution, and quadtree distribution with a near-fault data gap of 10 km

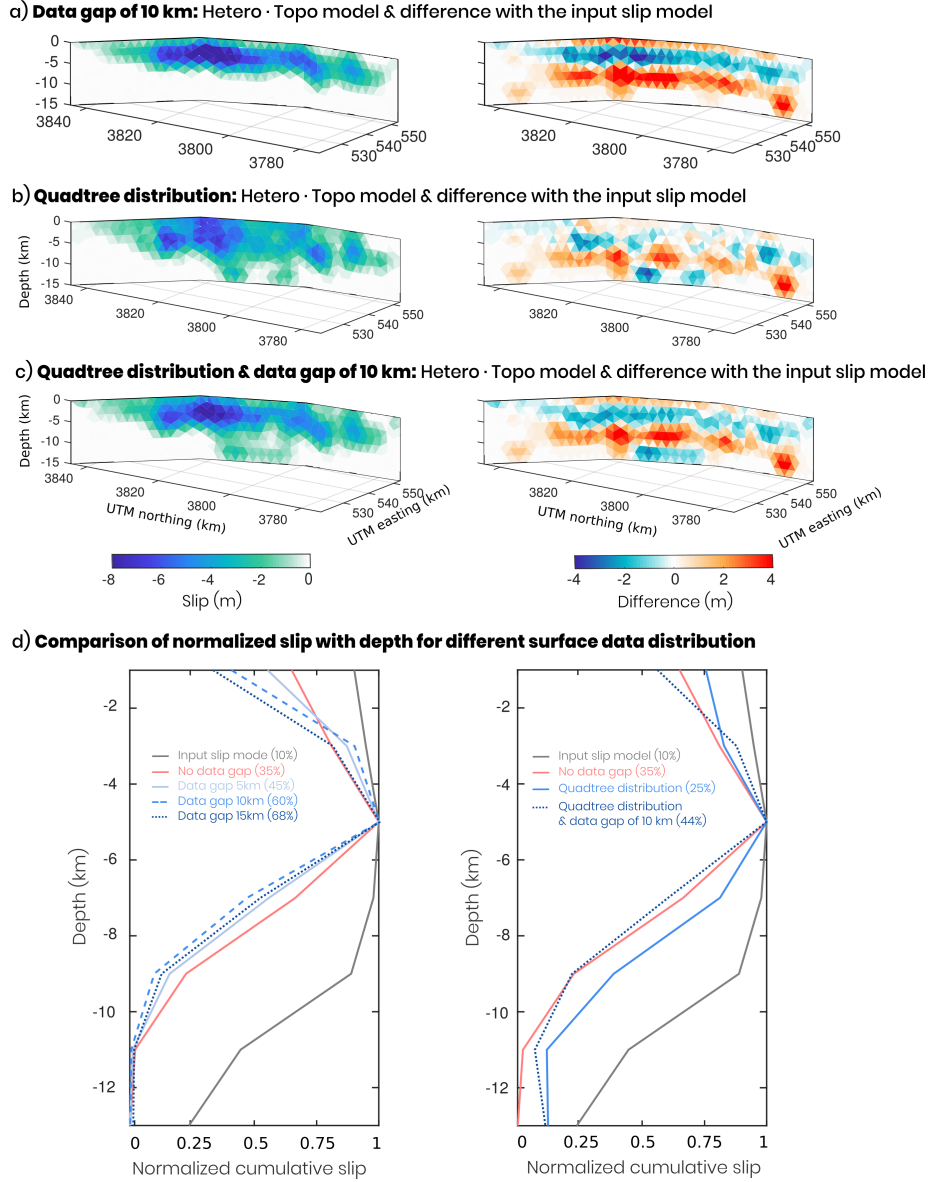


Figure 4: Impact of surface data distribution on the hetero-topo slip model. (a-c) Left side: Retrieved slip models obtained from the inversion of the hetero-topo data with a data gap of 10 km around the fault, a quadtree distribution, and both, respectively. Right side: Difference between the input and retrieved slip models. The retrieved slip models with a data gap of 5 and 15 km are shown in Figure S7. (d) Normalized cumulative slip with depth for the input slip model and the hetero-topo models inferred with a data gap around the fault of 5, 10, and 15 km (left side) and with a quadtree distribution of surface data, and both a quadtree distribution of surface data and a data gap of 10 km around the fault (right side). The amount of SSD for each model is indicated in brackets in the legend.

width).

The results for noise having a correlation length of 5 km are shown in Figures 5, S13, and S14; and in the animated figures available in the electronic supplements of this paper. Figure S13 shows the average slip models and the associated standard deviations obtained from the inversion of the homo-flat data with synthetic noise amplitude of 1 cm and 10 cm and for the different surface data distribution tested. The difference between the average slip model and the equivalent model obtained without noise is also shown. Figure S14 is the equivalent of Figure S13 for the hetero-topo case. The animated figures shows the 300 slip models inferred for each case. Figure 5 shows the statistics of the SSDs inferred from the 300 slip models for the different cases and for a noise correlation length and amplitude of 5km and 5cm, respectively. Results for noise correlation lengths of 2 km and 10 km are shown in Figures S15 and S16, respectively.

Whatever the tested medium (i.e. homo-flat or hetero-topo), the surface data distribution, or the noise amplitude, the average slip model looks similar to the equivalent model without noise (Figures S13 and S14). Both the standard deviation and the difference (with the equivalent model without noise) increase with noise amplitude. Concerning the SSD, for both the homo-flat and hetero-topo cases, the low amplitude noise (1 cm) has a low impact on the SSD (Figure 5). The mean SSD is similar to the equivalent test without noise and the range of SSD inferred is narrow (e.g.  $16.5 \pm 0.5\%$  and  $35\% \pm 0.4\%$  for the uniform homo-flat and uniform hetero-topo cases, respectively). As the noise amplitude increases, the mean SSD differs, albeit slightly, from the case without noise while the standard deviation of SSD

296 widens (e.g. from  $35\% \pm 0.4\%$  for an amplitude of 1 cm to  $33.6\% \pm 4\%$  for an  
 297 amplitude of 10 cm in the uniform hetero-topo case). The same holds when  
 298 the correlation length of the noise increases (Figures S15 and S16). Moreover,  
 299 the range of SSD is wider when there is a data gap close to the fault, in  
 300 particular for the homo-flat case ( $17.2 \pm 3\%$  for the uniform data distribution  
 301 and 5 cm noise and  $19 \pm 7\%$  for the distribution with the data gap and 5 cm  
 302 noise). Generally, noise affects the homo-flat cases more than hetero-topo  
 303 cases. This is shown by the range of inferred SSDs which is systematically  
 304 larger for homo-flat cases than hetero-topo cases, and by the larger variability  
 305 of the slip in the homo-flat models (see standard deviation plots in Figures  
 306 S13 and S14, and the animated figures available in the electronic supplements  
 307 of this paper). In the hetero-topo cases, the differences between the Green's  
 308 functions used to compute the synthetic data ( $\mathbf{G}_{HeTo}$ ) and the ones used in  
 309 the inversion ( $\mathbf{G}_{HoF}$ ), which are of similar order of magnitude as the noise but  
 310 spatially more coherent (Figure 1), have a larger influence on the retrieved  
 311 slip model than the synthetic noise. Consequently the noise has a lower  
 312 influence on the hetero-topo slip models than on the homo-flat slip models.  
 313 Finally, our results show that the homo-flat models can have SSD up to 40%  
 314 for a correlation length of 5 km and up to 46% for a correlation length of  
 315 10 km. Therefore, even when the medium is well described by the Green's  
 316 functions, slip models can exhibit artificial SSD solely due to noise in the  
 317 data.

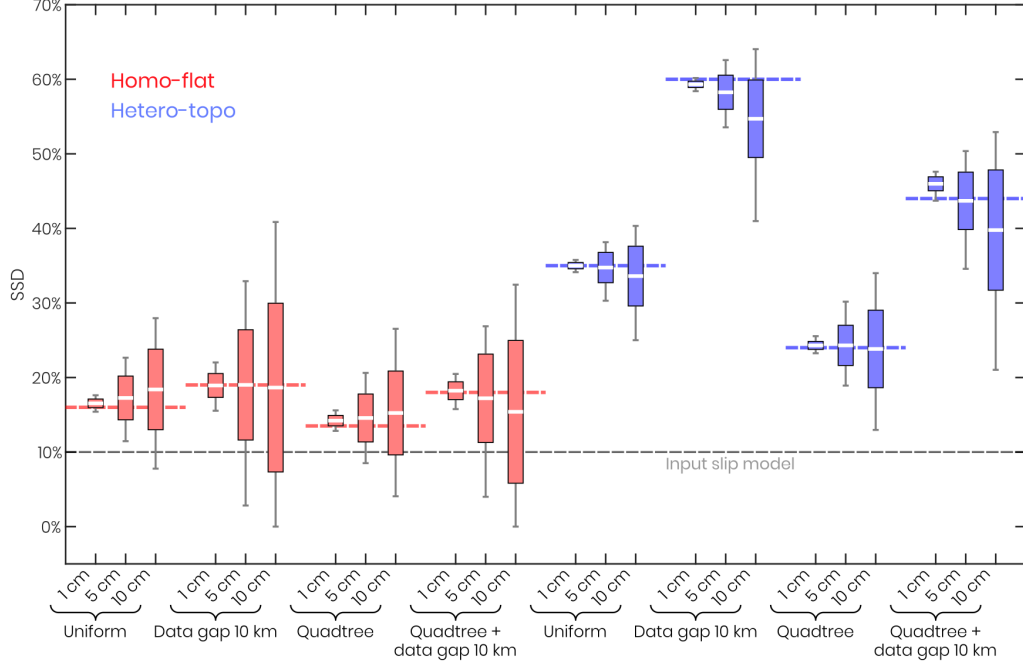


Figure 5: Impact of correlated noise with a correlation length of 5 km on the amount of SSD. Each box shows the statistics of the SSDs inferred from 300 inversions for a given medium (i.e. homo-flat or hetero-topo), a given data distribution (i.e uniform, 10 km wide data gap, quadtree, or quadtree and 10 km data gap), and a given noise amplitude (i.e. 1 cm, 5 cm or 10 cm). For each box, the white line represents the mean SSD, the box represents the standard deviation of the SSDs, and the bottom and top vertical lines extend to the 2th and 98th percentiles, respectively (meaning that  $\sim 95\%$  of the inferred SSDs lie between these two values). The red boxes are for homo-flat cases and the blue boxes are for hetero-topo cases. The maximum amplitude of noise and the surface data distribution are indicated on the x-axis. Finally, the red or blue horizontal dashed lines show the SSD of the equivalent model without noise and the gray horizontal dashed line shows the SSD of the input slip model. The results obtained for correlated noise with a correlation length of 2 km and 10 km are shown in Figures S15 and S16, respectively.

## 318 5. Impact of neglecting a damage zone on the amount of SSD

319 Major faults are surrounded by zones of highly damaged rocks associated  
320 with a reduction of the elastic moduli (e.g. Chester et al., 1993; Li et al., 2007;  
321 Fialko, 2004b). For the Landers fault zone, a damage zone ranging from 360-  
322 1100 m width with a reduction of the shear modulus of 80% compared to the  
323 surrounding medium has been inferred seismologically and geodetically (Li  
324 et al., 2007; Peng et al., 2003; Gombert et al., 2017). The depth extension  
325 of the damage zone is not well constrained and estimated values range from  
326  $\sim 3$  km to  $\sim 7$  km depth (Li et al., 2007; Peng et al., 2003). The resolution  
327 of the 3D velocity model we used in this study is too low for the damage  
328 zone to be visible. The potential effect of neglecting a damage zone on the  
329 retrieved slip model is thus not assessed in our previous tests. Therefore, in  
330 this section, we evaluate the impact of a damage zone on the distribution of  
331 slip with depth, and on the amount of SSD. We test damage zone widths of  
332 500 m and 1000 m centered on the fault, and we extend the damage zone to 7  
333 km depths. We apply a shear modulus in the damage zone equal to 20% of the  
334 shear modulus of the surrounding medium. Surface displacement differences  
335 between the homogeneous medium and the medium incorporating a damage  
336 zone are shown in Figure S17, and a comparison of profiles across the fault  
337 in the different mediums are shown in Figure S18. Significant differences  
338 are observed within 10 km of the fault;  $\sim 6.5$  cm for the 500 m damage  
339 zone, and  $\sim 9$  cm for the 1000 m damage zone (Figures S17 and S18). The  
340 profile comparison shows that when a damage zone is incorporated, a larger  
341 part of the deformation is accommodated within this damage zone (i.e. a  
342 higher gradient displacement within the damage zone compared with the

343 homogeneous case).

344     The impact of neglecting a damage zone on the distribution of slip with  
345 depth has already been evaluated by Barbot et al. (2008), who showed that  
346 neglecting the damage zone mainly impacts the overall slip amplitude on the  
347 fault. However, a mismodelled damage zone coupled with a lack of near-fault  
348 data could lead to an underestimation of the slip at shallow depths as the  
349 amplitude of the surface displacement outside the damage zone is lower in  
350 the damage zone model than in the homogeneous model (see Figure S18).  
351 We thus run two inversions, one incorporating data points within the damage  
352 zone, and the other with data points located only outside the damage zone.  
353 The mean retrieved slip with depth, as well as the cumulative slip with  
354 depth are shown in Figure S19. Whatever the surface data distribution,  
355 the slip amplitude of the damage zone models are generally lower than the  
356 slip amplitude of the input slip model (Figure S19a,c). When there are  
357 data points within the damage zone, the surface slip (0-1 km depth) is well  
358 retrieved (mean slip of 2.69 m, 2.70 m, and 2.65 m for the 500 m damage  
359 zone, 1000 m damage zone, and input slip models, respectively). However,  
360 when no data points are located within the damage zone, the surface slip is  
361 slightly underestimated (mean slip of 2.4 m and 2.3 m for the 500 m and 1000  
362 m damage zone models, respectively). Consequently, there is no artificial  
363 shallow slip deficit in the first case (SSD of 8%, 6%, and 10% for the 500  
364 m damage zone, damage zone 1000 m, and input slip models, respectively,  
365 Figure S19b) and a slight artificial SSD in the second case (SSD of 16%,  
366 16%, and 10% for the 500 m damage zone, damage zone 1000 m, and input  
367 slip models respectively, Figure S19d). The impact of neglecting a damage

368 zone on the SSD is therefore significantly less important than the impact of  
369 neglecting the variations in elastic structure with depth (Figure 3).

## 370 6. Discussion

### 371 6.1. *Neglecting the variation in elastic properties can produce artificial SSD*

372 Results presented in section 2 show that, in the example considered here,  
373 the topography has a moderate impact on the surface displacements (Fig-  
374 ure 1). Consequently, neglecting the contribution of topography when in-  
375 verting for the slip at depth leads to a limited bias on the inferred slip model  
376 (Figure 2c). The only noticeable difference is that the slip extends deeper  
377 in the retrieved slip model than in the input slip model (Figure 2c and 3).  
378 The moderate impact of the topography is due to the limited topographic  
379 variation across the Landers region, with a maximum altitude difference on  
380 both sides of the fault of around 200 m. On the contrary, the variations  
381 in elastic properties have a significant impact on the surface displacements  
382 (Figure 1) and neglecting them leads to significant bias in the slip model  
383 (Figure 2d). In particular, our results show that, by neglecting variations in  
384 elastic properties, we significantly overestimate slip at  $\sim 4.5$  km depth, which  
385 leads to an increase in shallow slip deficit of 25% (Figure 3).

386 The elastic properties inferred from the velocity model used in section 2  
387 vary mainly with depth, whereas the lateral variations are more moderate  
388 (Figure S1). Thus, we should obtain results similar to those presented in  
389 section 2 (i.e. Figure 2d) if we use a 1-D layered velocity model to compute  
390 the synthetic data. To confirm this and to evaluate which features of the  
391 layered medium control our results, we compute the surface displacements

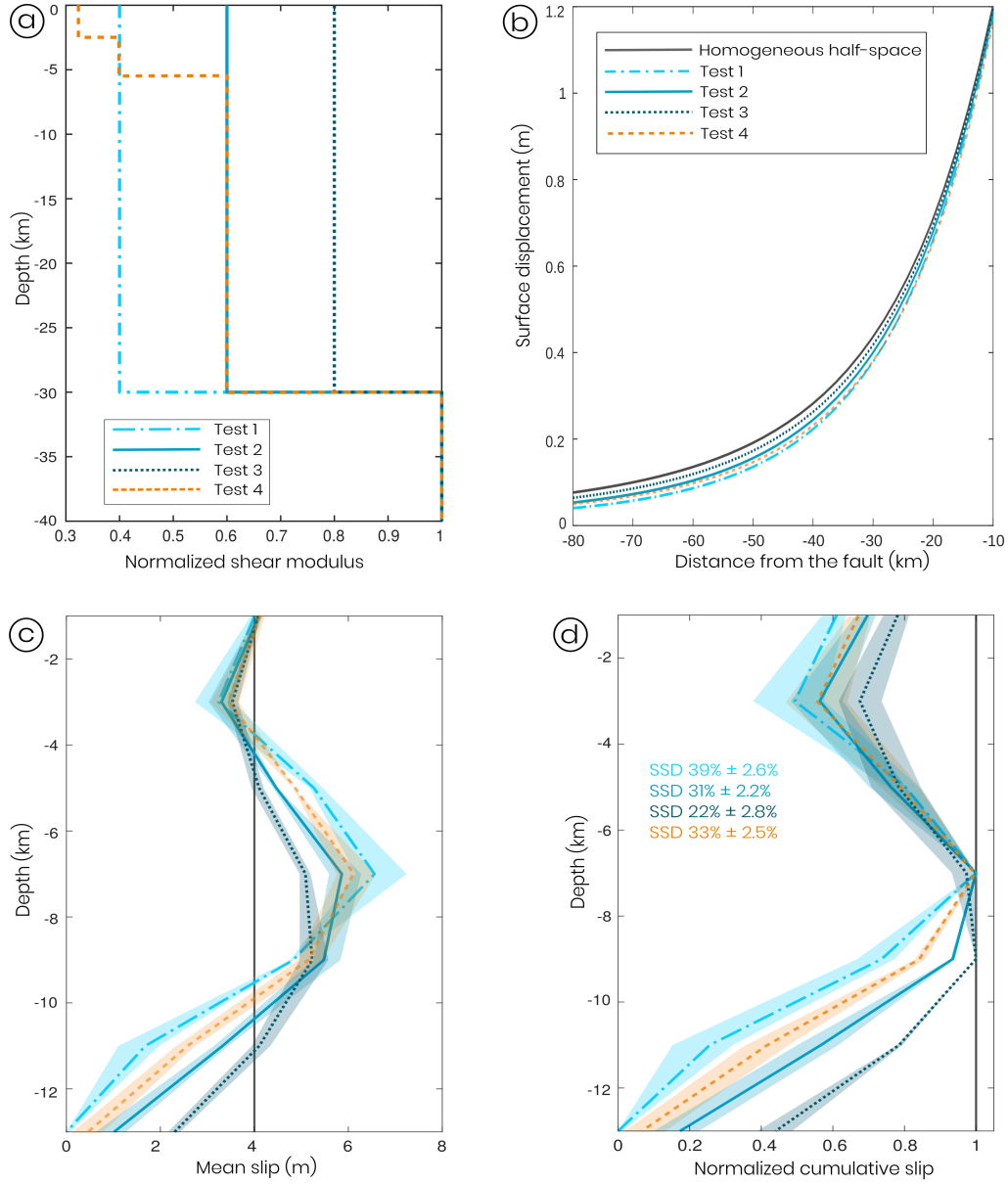


Figure 6: (a) Shear modulus as a function of depth in tests 1–4 (see text for details). The shear modulus is normalized by the modulus of the underlying half-space. (b) Comparison of surface displacement profiles produced by 4 m of uniform slip in a homogeneous half-space and in the layered mediums of tests 1–4. (c) Mean slip with depth of the retrieved slip model in the tests 1–4. (d) Corresponding curves of normalized cumulative slip with depth.

392 resulting from 4 m of uniform slip on a 100 km long strike-slip fault in various  
 393 layered mediums, and invert them using Green’s function calculated in a  
 394 homogeneous half-space (Okada, 1992). We use a uniform input slip to avoid  
 395 any potential effects resulting from the variation of slip with depth, or along-  
 396 strike. Moreover, for practical reasons, we use the code of Wang et al. (2003)  
 397 rather than Pylith to compute the synthetic displacements in the various  
 398 layered mediums. We test 4 layered mediums. The three first mediums are  
 399 composed of one weak layer of 30 km width overlying a homogeneous half-  
 400 space (Tests 1-3, Figure 6a), with a shear modulus ratio between the shallow  
 401 and the deep layer of 0.4, 0.6, and 0.8. The fourth medium is inferred from  
 402 the seismic velocity model of the Landers area (Share et al., 2019), and is  
 403 composed of 3 layers (Figure 6a) with widths of 2.5, 3, and 24.5 km and a  
 404 shear modulus ratio with respect to the underlying half-space of 0.32, 0.40,  
 405 and 0.6 (Test 4, Figure 6a). The mean retrieved slip with depth for tests 1-4,  
 406 as well as the corresponding curves of cumulative slip with depth, are shown  
 407 in Figures 6c and 6d. All retrieved slip models have the same characteristics  
 408 as the hetero-topo model: (1) the sub-surface slip is well retrieved, (2) slip at  
 409 mid-depths of 6-8 km is overestimated, and (3) slip at greater depths (below  
 410  $\sim 10$  km) is underestimated (Figure 6c). Consequently, all models display an  
 411 artificial shallow slip deficit (Figure 6d). The amount of SSD depends on the  
 412 shear modulus ratio between the weak and rigid layers; the lower the ratio,  
 413 the higher the SSD. The inferred SSD varies from 39% to 22% for ratios  
 414 ranging from 0.4 to 0.8 (Tests 1-3, Figure 6d).

415 The retrieved slip model in test 4 is very similar to the retrieved slip model  
 416 of test 2 in the shallowest half of the fault (0–8 km depth). Consequently the

417 amount of artificial SSD in tests 2 and 4 is very similar (31% versus 33%).  
418 Given, the only difference between those tests is the presence of the two  
419 shallow layers in test 4, this result suggests that the strong rigidity contrast  
420 at depth (i.e. the Moho), far below the down-dip extent of the fault, exerts  
421 the dominant control on the retrieved fault slip distribution with depth.  
422 This effect may (in part) account for the discrepancy seen in the depth of  
423 slip inferred from geodetic vs seismological observations (e.g. 2016 Kaikoura  
424 earthquake; Cesca et al., 2017; Hamling et al., 2017; Hollingsworth et al.,  
425 2017; Wang et al., 2018).

426 The difference in terms of surface displacements between a homogeneous  
427 half-space and a layered medium have long been known (Savage, 1987; Segall,  
428 2010), and analytical models show that, for homogeneous slip located in  
429 the weak layer, the surface displacement decreases more rapidly away from  
430 the fault (i.e. the deformation is more concentrated close to the fault) in  
431 the layered medium compared with the homogeneous half-space (Figure 6b).  
432 Considering this, it is not obvious how neglecting the elastic properties when  
433 inverting for fault slip leads to an overestimation of the slip at depth. Indeed,  
434 the only expected effect would be to underestimate the fault width (Segall,  
435 2010). If the only parameters that we invert for are the fault width and a  
436 uniform slip, we would obtain the correct slip but with a shallower fault depth  
437 (Figure S20). However, when the slip is allowed to vary with depth, the slip  
438 model that best fits the data is a model with an increase of slip at mid-depths,  
439 while the shallow slip is correctly retrieved because it is constrained by near-  
440 field surface observation. Therefore, when normalized to the maximum slip,  
441 the slip model displays an artificial shallow slip deficit.

Our findings suggest that an inversion accounting for a layered model should not produce significant artificial shallow slip deficit. To confirm this, we invert the hetero-topo data using Green's functions computed in the 4-layered medium shown in Figure 6a (which is a good representation of the variations in elastic properties for the Landers area). The retrieved slip model and the curve of cumulative slip with depth show that the slip distribution is quite well retrieved and has an artificial SSD significantly reduced compared to the model obtained with the homogeneous Green's functions (16% versus 35%, Figure S21).

## 6.2. *Shallow slip deficit: a real feature or modeling artifact?*

It has long been recognized that coseismic slip at depth is often higher than the surface slip (e.g Thatcher & Bonilla, 1989; Fialko et al., 2005; Dolan & Haravitch, 2014). This observation has raised several questions: what are the mechanical processes that prevent fault slip from propagating fully to the surface, and how and when in the seismic cycle is this deficit of slip accommodated? Is the SSD accommodated on or off the main fault? Is the SSD an artifact? Answering these questions is essential for fully understanding how faults rupture the crust in response to tectonic loading. A more complete understanding of faulting in the shallow crust is of great importance to society given the key role the latter plays in modulating strong ground motions during earthquakes. Moreover, better characterization of how faults rupture the shallow crust is essential for the correct estimation of seismic hazard using probabilistic approaches, especially when incorporating Quaternary-derived fault slip rates (Dolan & Haravitch, 2014). Over longer times-scales, structural models of fault zone evolution, and the role played by on- vs off-fault

467 processes in fault growth, are both subject to mechanical processes operating  
468 over individual earthquakes.

469 We show that neglecting the variations with depth of elastic properties  
470 can produce artificial SSD by overestimating the slip at depth. Additionally,  
471 we show that a lack of near-fault data further increases the amount of arti-  
472 ficial SSD by reducing the slip in the subsurface (see also Xu et al., 2016).  
473 Our results imply that SSD inferred in previous inversion studies based on a  
474 homogeneous half-space approach could be significantly overestimated, and  
475 perhaps even non-existent (e.g. Funning et al., 2007; Sudhaus & Jonsson,  
476 2011; Hamling et al., 2017). However, substantial SSD has also been in-  
477 ferred from inversion studies that use more realistic 1D forward models, and  
478 which incorporate near-fault data (e.g. Simons et al., 2002; Wei et al., 2011;  
479 Gombert et al., 2017). Moreover, Simons et al. (2002) inferred two slip mod-  
480 els for the Hector-Mine earthquake, one using an elastic half-space and the  
481 other using a layered elastic medium. They found that both models have  
482 an equivalent amount of SSD (the SSD of the layered model being slightly  
483 larger than the SSD of the homogeneous model). In that case, the inferred  
484 SSD could thus be real and due (in part) to off-fault deformation in the  
485 elasto-plastic uppermost crust (Kaneko & Fialko, 2011; Roten et al., 2017,  
486 e.g.). Nevertheless, the dynamic simulations of Kaneko & Fialko (2011) fail  
487 to predict the correct amount of SSD inferred from kinematic source inver-  
488 sions. Furthermore the simulations of Roten et al. (2017) predict 45% of  
489 SSD, albeit only in the uppermost 300 m of the crust, whereas SSD inferred  
490 from kinematic source inversion is generally located in the uppermost 3 km.  
491 Therefore, these observations indicate that the extent to which SSD is a

492 modeling artifact or not is still not fully understood. However, other factors  
 493 can produce artificial SSD. In particular, we show that even if the medium  
 494 is perfectly represented by the Green's functions, artificial SSD can arise  
 495 solely due to the presence of correlated noise in the data. Both InSAR and  
 496 optical correlation data contain spatially correlated noise. For C-band inter-  
 497 ferograms (e.g. Sentinel-1), correlated noise is mainly due to tropospheric  
 498 delays and is typically several centimeters (e.g. Zebker et al., 1997; Hanssen  
 499 et al., 1999). For L-band interferograms (e.g. ALOS-2), the noise due to  
 500 ionospheric delay is more important and can reach tens of centimeters (e.g.  
 501 Gray et al., 2000). Techniques exist to correct (partially) the contribution  
 502 of the tropospheric and ionosphere to the interferometric phase (e.g. Jolivet  
 503 et al., 2011; Gomba et al., 2015). However, for coseismic studies of large  
 504 shallow earthquakes, those errors are usually not corrected because the noise  
 505 is significantly smaller than the coseismic signal, and so it is assumed that  
 506 the final slip model will not be significantly biased. In optical correlation  
 507 data, noise is correlated over shorter distances than with InSAR although  
 508 the amplitude is typically higher (reaching several meters in some cases) and  
 509 the noise is more difficult to correct. Here we show that with a maximum  
 510 noise amplitude equal to only 2% of the maximum displacement, significant  
 511 artificial SSD can be inferred, even when the correlation length of the noise is  
 512 short. Our study therefore underlines the necessity to systematically infer  
 513 noise-related robustness of slip models in inversion studies. For example, es-  
 514 timation of the model parameter uncertainties arising from data noise can  
 515 be done by performing repeated optimizations of the data corrupted by syn-  
 516 thetic error simulations with the same characteristics as the real data noise

517 (e.g. Sudhaus & Jonsson, 2009). Approaches that discretize the surface data  
518 and fault plane in a way that minimizes the impact of noise on the slip model  
519 can also be used (e.g. Ziv, 2016; Magen et al., 2020).

520 We also explore the effect of neglecting the reduction in the shear modulus  
521 around the fault (compliant zone). Our results are consistent with those of  
522 Barbot et al. (2008) and show that if there are data close to the fault (i.e.  
523 within the damage zone), the main effect of neglecting a 0.5 and 1 km wide  
524 damage zone (shear modulus ratio of 0.2) is to underestimate slip on the fault  
525 plane. However, if there are no data close to the fault, a slight artificial SSD  
526 is produced, but largely smaller than the one produced when the variations  
527 of elastic properties with depth are neglected.

528 Unfortunately, our ability to resolve the true fault slip distribution, partic-  
529 ularly with depth, is limited by the inherently ill-posed nature of the inverse  
530 problem. Many solutions to this problem exist (i.e. it is non-unique), and the  
531 final optimal slip model depends strongly on numerous factors, such as the  
532 quantity, distribution, and quality of surface data (e.g. Delouis et al., 2002;  
533 Ziv, 2016; Marchandon et al., 2018), the assumed fault geometry (e.g. Ragon  
534 et al., 2018), the discretization of the fault plane (e.g. Page et al., 2009; Atzori  
535 et al., 2012; Magen et al., 2020), the smoothing applied (e.g. Jonsson et al.,  
536 2002), the capacity of the forward model to accurately represent the rheology  
537 of the Earth (e.g. Duputel et al., 2014), and whether or not gravity is taken  
538 into account (e.g. Gómez et al., 2017). Different inversion schemes aim at  
539 addressing some of these issues. For example, Bayesian inversion schemes  
540 (e.g. Minson et al., 2013; Duputel et al., 2014; Nocquet, 2018) determine the  
541 range of all plausible slip models that are consistent with the observations

542 and a priori knowledge of the crustal rheology, thus allowing the uncertainty  
 543 of each inverted parameter to be assessed (at the expense of increased com-  
 544 putational cost). Other methods discretize the data and the fault plane in a  
 545 way that optimizes the condition of the inverse problem (Ziv, 2016; Magen  
 546 et al., 2020), such that the effect of noise on the model is minimized. Nev-  
 547 ertheless, although these approaches can estimate the uncertainty or reduce  
 548 the error in the shallow part of the slip model, they will not capture the bias  
 549 introduced if the rheology or topography are not considered in the inversion.  
 550 Future studies may aim to develop new ways to invert for fault slip which  
 551 integrate a range of parameters such as measurement noise, rheology, topog-  
 552 raphy, gravity, data discretization, off-fault damage, non-elastic deformation  
 553 mechanisms, hydro-mechanical effects, and fault geometry uncertainty.

### 554 *6.3. Implications for using the Okada solution to resolve fault slip*

555 Our study implies that even a well-studied earthquake with good InSAR,  
 556 GPS, optical correlation, and field data can still yield substantial error in the  
 557 final slip distribution, particularly at depth, when modelled using the Okada  
 558 solution. Despite these limitations, traditional inversion approaches based  
 559 on the Okada solution are nevertheless a powerful way to quickly resolve the  
 560 first order aspects of the fault slip distribution. However, when knowledge of  
 561 the slip-variability is required (either along-strike, or down-dip), e.g. when  
 562 characterizing the evolution of stresses in fault zones throughout the seismic  
 563 cycle, one may improve substantially on traditional inversion approaches by  
 564 incorporating FEM-based methods for computing the Green’s functions (e.g.  
 565 PyLITH), thus accounting for local rheology and topographic relief of the  
 566 source region (data which is readily available in many regions).

567 It is also worth noting that our analysis is focused on a strike-slip fault  
568 example, in which there is only limited topographic relief or lateral variation  
569 in the elastic structure across the fault. The Landers earthquake therefore  
570 represents a case where the Okada solution would be expected to perform  
571 well, with minimal bias due to errors in the Green’s functions. This is not the  
572 case in our experiments, therefore highlighting how topography and rheology  
573 can play an important role in our ability to accurately resolve slip on the  
574 shallow regions of crustal faults generally. In the case of strike-slip faults,  
575 where the lateral variations in elastic properties are limited, using a 1D strat-  
576 ified model could be sufficient and a significant improvement with respect to  
577 Okada.

578 In the case of subduction megathrusts, where both topography and rhe-  
579 ology (and gravity, e.g. Gómez et al. (2017)) can vary significantly more  
580 than for Landers, and where large gaps in displacement data occur close to  
581 the surface expression of the fault (i.e. the near-field region), it is likely that  
582 fault slip inversions based on Okada are highly biased along their up-dip sec-  
583 tions. The distribution of slip in large megathrust earthquakes may therefore  
584 generally underestimate co-seismic slip in the shallowest crust, which will in  
585 turn impact the estimated seismic (and tsunamigenic) hazard posed by such  
586 structures (e.g. Almeida et al., 2018). Within the continents, where we have  
587 better spatial coverage of the near-field region, we are only just starting to in-  
588 corporate detailed near-field geodetic data into slip inversions (e.g. Gombert  
589 et al., 2017). However, to do so requires a correspondingly more detailed  
590 (and accurate) shallow fault geometry, and velocity model; if such informa-  
591 tion is lacking, it will ultimately limit our ability to accurately resolve the

592 shallow slip distribution.

## 593 7. Conclusion

594 In this study, we investigate the impact of neglecting the medium com-  
595 plexities (3D variations in elastic properties and topography) on the results  
596 of fault slip inversions and, in particular, on the amount of slip at shallow  
597 depths. Using the 1992 Landers earthquake as a test case, we show that ne-  
598 glecting the moderate topography variations of the Landers area has a quite  
599 limited influence on the retrieved slip model, although it does impact the  
600 extent of the slip at depth. On the contrary, neglecting the variations in  
601 elastic properties significantly biases the retrieved slip model and introduces  
602 25% artificial SSD by overestimating the slip at depth. Using a toy model,  
603 we show that neglecting the variations in elastic properties with depth is  
604 responsible for the artificial SSD, and that the contrast of rigidity between  
605 the crust and the mantle controls the amount of artificial SSD (whereas the  
606 variation in rigidity within the crust has a more limited impact). We also  
607 assess the impact of neglecting a damage zone and find that it has a rel-  
608 atively limited effect on the amount of SSD. We further show that a lack  
609 of data coverage around the fault increases the amount of artificial SSD by  
610 decreasing the slip at shallow depths, whereas a quadtree distribution of sur-  
611 face data tends to reduce the artificial SSD. Finally, we explore the impact  
612 of correlated noise on our results and show that noise levels as low as 5%  
613 of the maximum displacement can lead to substantial SSD. Our results sug-  
614 gest that the SSD inferred from previous inversion studies based on Okada  
615 are likely overestimated (maybe even non-existent). Therefore, Okada should

not be used when knowledge of the slip-variability with depth is sought, even in areas with limited variation in topography and elastic properties, like the Landers area. Moreover, noise-related model uncertainties should be systematically estimated to avoid misinterpretation of slip model features. Finally, we argue that the origin of SSD can only be fully understood with a more complete knowledge of all the processes and parameters that govern fault slip in the upper crust (e.g. off-fault plastic-deformation, hydro-mechanical effects, gravity, 3D structure of faults, etc).

## Acknowledgment

The slip model of Hernandez et al. (1999) has been retrieved from the SRCMOD website (<http://equake-rc.info/SRCMOD/searchmodels/viewmodel/s1992LANDER01HERN/>). This research was supported by the CNES (French spatial agency) through the funding of Mathilde Marchandon’s post-doc and by the INSU TelluS program. We are grateful to Z. Duputel and an anonymous reviewer for their constructive and thorough comments that greatly helped us to improve our manuscript.

## References

- Aagaard, B. T., Knepley, M. G., & Williams, C. A. (2013). A domain decomposition approach to implementing fault slip in finite-element models of quasi-static and dynamic crustal deformation. *Journal of Geophysical Research: Solid Earth*, 118, 3059–3079.
- Almeida, R., Lindsey, E. O., Bradley, K., Hubbard, J., Mallick, R., & Hill, E. M. (2018). Can the updip limit of frictional locking on megathrusts be

639 detected geodetically? quantifying the effect of stress shadows on near-  
640 trench coupling. *Geophysical Research Letters*, 45, 4754–4763.

641 Atzori, S., Tolomei, C., Antonioli, A., Boncori, J. P. M., Bannister, S.,  
642 Trasatti, E., Pasquali, P., & Salvi, S. (2012). The 2010–2011 Canter-  
643 bury, New Zealand, seismic sequence: Multiple source analysis from In-  
644 SAR data and modeling. *Journal of Geophysical Research*, 117, 1–16.  
645 doi:10.1029/2012JB009178.

646 Barbot, S., Fialko, Y., & Sandwell, D. (2008). Effect of a compliant fault  
647 zone on the inferred earthquake slip distribution. *Journal of Geophysical*  
648 *Research: Solid Earth*, 113.

649 Brocher, T. M. (2005). Empirical relations between elastic wavespeeds and  
650 density in the earth’s crust. *Bulletin of the seismological Society of Amer-*  
651 *ica*, 95, 2081–2092.

652 Cesca, S., Zhang, Y., Mouslopoulou, V., Wang, R., Saul, J., Savage, M.,  
653 Heimann, S., Kufner, S.-K., Oncken, O., & Dahm, T. (2017). Complex  
654 rupture process of the mw 7.8, 2016, kaikoura earthquake, new zealand,  
655 and its aftershock sequence. *Earth and Planetary Science Letters*, 478,  
656 110–120.

657 Chester, F. M., Evans, J. P., & Biegel, R. L. (1993). Internal structure and  
658 weakening mechanisms of the san andreas fault. *Journal of Geophysical*  
659 *Research: Solid Earth*, 98, 771–786.

660 Coleman, T. F., & Li, Y. (1992). A reflective Newton method for minimizing

661 a quadratic function subject to bounds on some of the variables. *Journal*  
662 *on optimization*, (pp. 1–37).

663 Delouis, B., Giardini, D., Lundgren, P., & Salichon, J. (2002). Joint Inversion  
664 of InSAR, GPS, Teleseismic, and Strong-Motion Data for the Spatial and  
665 Temporal Distribution of Earthquake Slip : Application to the 1999 Izmit  
666 Mainshock. *Bulletin of Seismological Society of America*, 92, 278–299.

667 Dolan, J. F., & Haravitch, B. D. (2014). How well do surface slip mea-  
668 surements track slip at depth in large strike-slip earthquakes? The im-  
669 portance of fault structural maturity in controlling on-fault slip ver-  
670 sus off-fault surface deformation. *Earth and Planetary Science Letters*,  
671 388, 38–47. URL: <http://dx.doi.org/10.1016/j.epsl.2013.11.043>.  
672 doi:10.1016/j.epsl.2013.11.043.

673 Duputel, Z., Agram, P. S., Simons, M., Minson, S. E., & Beck, J. L. (2014).  
674 Accounting for prediction uncertainty when inferring subsurface fault slip.  
675 *Geophysical Journal International*, 197, 464–482.

676 Fialko, Y. (2004a). Evidence of fluid-filled upper crust from observations  
677 of postseismic deformation due to the 1992 mw7. 3 landers earthquake.  
678 *Journal of Geophysical Research: Solid Earth*, 109.

679 Fialko, Y. (2004b). Probing the mechanical properties of seismically active  
680 crust with space geodesy: Study of the coseismic deformation due to the  
681 1992 mw7. 3 landers (southern california) earthquake. *Journal of Geophys-  
682 ical Research: Solid Earth*, 109.

683 Fialko, Y., Sandwell, D., Simons, M., & Rosen, P. (2005). Three-dimensional  
684 deformation caused by the Bam, Iran, earthquake and the origin of shallow  
685 slip deficit. *Nature*, *435*, 295–299. doi:10.1038/nature03425.

686 Funning, G. J., Parsons, B., & Wright, T. J. (2007). Fault slip in  
687 the 1997 Manyi, Tibet earthquake from linear elastic modelling of In-  
688 SAR displacements. *Geophysical Journal International*, (pp. 988–1008).  
689 doi:10.1111/j.1365-246X.2006.03318.x.

690 Gomba, G., Parizzi, A., De Zan, F., Eineder, M., & Bamler, R. (2015).  
691 Toward operational compensation of ionospheric effects in sar interfero-  
692 grams: The split-spectrum method. *IEEE Transactions on Geoscience*  
693 *and Remote Sensing*, *54*, 1446–1461.

694 Gombert, B., Duputel, Z., Jolivet, R., Doubre, C., Rivera, L., & Simons, M.  
695 (2017). Revisiting the 1992 Landers earthquake: a Bayesian exploration of  
696 co-seismic slip and off-fault damage. *Geophysical Journal International*, .  
697 doi:10.1093/gji/ggx455.

698 Gómez, D. D., Bevis, M., Pan, E., & Smalley Jr, R. (2017). The influence  
699 of gravity on the displacement field produced by fault slip. *Geophysical*  
700 *Research Letters*, *44*, 9321–9329.

701 Gray, A. L., Mattar, K. E., & Sofko, G. (2000). Influence of ionospheric  
702 electron density fluctuations on satellite radar interferometry. *Geophysical*  
703 *Research Letters*, *27*, 1451–1454.

704 Hamling, I. J., Hreinsdóttir, S., Clark, K., Elliott, J., Liang, C., Fielding,  
705 E., Litchfield, N., Villamor, P., Wallace, L., Wright, T. J. et al. (2017).

706     Complex multifault rupture during the 2016 mw 7.8 kaikōura earthquake,  
707     new zealand. *Science*, *356*, eaam7194.

708     Hanssen, R. F., Weckwerth, T. M., Zebker, H. A., & Klees, R. (1999). High-  
709     resolution water vapor mapping from interferometric radar measurements.  
710     *Science*, *283*, 1297–1299.

711     Hernandez, B., Cotton, F., & Campillo, M. (1999). Contribution of radar  
712     interferometry to a two-step inversion of the kinematic process of the 1992  
713     landers earthquake. *Journal of Geophysical Research: Solid Earth*, *104*,  
714     13083–13099.

715     Hollingsworth, J., Lingling, Y., & Avouac, J.-p. (2017). Dynamically trig-  
716     gered slip on a splay fault in the Mw 7.8, 2016 Kaikoura (New Zealand)  
717     earthquake. *Geophysical Research Letters*, (pp. 3517–3525). doi:10.1002/  
718     2016GL072228.

719     Huang, M.-H., Fielding, E. J., Dickinson, H., Sun, J., Gonzalez-Ortega, J. A.,  
720     Freed, A. M., & Bürgmann, R. (2017). Fault geometry inversion and slip  
721     distribution of the 2010 mw 7.2 el mayor-cucapah earthquake from geodetic  
722     data. *Journal of Geophysical Research: Solid Earth*, *122*, 607–621.

723     Jolivet, R., Grandin, R., Lasserre, C., Doin, M.-P., & Peltzer, G. (2011).  
724     Systematic insar tropospheric phase delay corrections from global meteo-  
725     rological reanalysis data. *Geophysical Research Letters*, *38*.

726     Jonsson, S., Zebker, H., Segall, P., & Amelung, F. (2002). Fault Slip Distribu-  
727     tion of the 1999 Mw 7.1 Hector Mine, California, Earthquake, Estimated

728 from Satellite Radar and GPS Measurements. *Bulletin of Seismological*  
729 *Society of America*, 92, 1377–1389.

730 Kaneko, Y., & Fialko, Y. (2011). rupture simulations with elasto-plastic  
731 off-fault response. *Geophysical Journal International*, 186, 1389–1403.  
732 doi:10.1111/j.1365-246X.2011.05117.x.

733 Langer, L., Gharti, H. N., & Tromp, J. (2019). Impact of topography and  
734 three-dimensional heterogeneity on coseismic deformation. *Geophysical*  
735 *Journal International*, 217, 866–878.

736 Li, H., Zhu, L., & Yang, H. (2007). High-resolution structures of the landers  
737 fault zone inferred from aftershock waveform data. *Geophysical Journal*  
738 *International*, 171, 1295–1307.

739 Li, Y., Bürgmann, R., & Zhao, B. (2020). Evidence of fault immaturity from  
740 shallow slip deficit and lack of postseismic deformation of the 2017 m w 6.5  
741 jiuzhaigou earthquake. *Bulletin of the Seismological Society of America*, .

742 Lindsey, E. O., Fialko, Y., Bock, Y., Sandwell, D. T., & Bilham, R. (2014).  
743 Localized and distributed creep along the southern san andreas fault. *Jour-*  
744 *nal of Geophysical Research: Solid Earth*, 119, 7909–7922.

745 Magen, Y., Ziv, A., Inbal, A., Baer, G., & Hollingsworth, J. (2020). Fault  
746 rerupture during the july 2019 ridgecrest earthquake pair from joint slip  
747 inversion of insar, optical imagery, and gps. *Bulletin of the Seismological*  
748 *Society of America*, 110, 1627–1643.

749 Marchandon, M., Vergnolle, M., Cavali, O., Sudhaus, H., & Hollingsworth,  
750 J. (2018). Earthquake sequence in the NE Lut, Iran : Observations from

multiple space geodetic techniques. *Geophysical Journal International*,  
(pp. 1–37).

Minson, S. E., Simons, M., & Beck, J. L. (2013). Bayesian inversion for  
finite fault earthquake source models I—theory and algorithm. *Geophysical  
Journal International*, *194*, 1701–1726. doi:10.1093/gji/ggt180.

Nocquet, J.-M. (2018). Stochastic static fault slip inversion from geodetic  
data with non-negativity and bound constraints. *Geophysical Journal In-  
ternational*, *214*, 366–385.

Okada, Y. (1992). Internal deformation due to shear and tensile faults in a  
half-space. *Bulletin of Seismological Society of America*, (pp. 1018–1040).

Page, M. T., Custo, S., Archuleta, R. J., & Carlson, J. M. (2009). Con-  
straining earthquake source inversions with GPS data: 1. Resolution-  
based removal of artifacts. *Journal of African Earth Sciences*, *114*, 1–13.  
doi:10.1029/2007JB005449.

Peng, Z., Ben-Zion, Y., Michael, A. J., & Zhu, L. (2003). Quantitative anal-  
ysis of seismic fault zone waves in the rupture zone of the 1992 landers,  
california, earthquake: evidence for a shallow trapping structure. *Geophys-  
ical Journal International*, *155*, 1021–1041.

Ragon, T., Sladen, A., & Simons, M. (2018). Accounting for uncertain fault  
geometry in earthquake source inversions—i: theory and simplified applica-  
tion. *Geophysical Journal International*, *214*, 1174–1190.

Reid, H. F. (1910). *The california earthquake of April 18, 1906. Volume 2:  
The mechanics of the earthquake*. Technical Report.

774 Ross, Z. E., Idini, B., Jia, Z., Stephenson, O. L., Zhong, M., Wang, X.,  
775 Zhan, Z., Simons, M., Fielding, E. J., Yun, S.-H. et al. (2019). Hierarchical  
776 interlocked orthogonal faulting in the 2019 ridgecrest earthquake sequence.  
777 *Science*, *366*, 346–351.

778 Roten, D., Olsen, K., & Day, S. (2017). Off-fault deformations and shallow  
779 slip deficit from dynamic rupture simulations with fault zone plasticity.  
780 *Geophysical Research Letters*, *44*, 7733–7742.

781 Rousset, B., Jolivet, R., Simons, M., Lasserre, C., Riel, B., Milillo, P., Çakir,  
782 Z., & Renard, F. (2016). An aseismic slip transient on the north anatolian  
783 fault. *Geophysical Research Letters*, *43*, 3254–3262.

784 Savage, J. C. (1987). Effect of crustal layering upon dislocation modeling.  
785 *Journal of Geophysical Research: Solid Earth*, *92*, 10595–10600.

786 Segall, P. (2010). *Earthquake and volcano deformation*. Princeton University  
787 Press.

788 Share, P.-E., Guo, H., Thurber, C. H., Zhang, H., & Ben-Zion, Y. (2019).  
789 Seismic imaging of the southern california plate boundary around the  
790 south-central transverse ranges using double-difference tomography. *Pure*  
791 *and Applied Geophysics*, *176*, 1117–1143.

792 Simons, M., Fialko, Y., & Rivera, L. (2002). Coseismic Deformation from  
793 the 1999 M w 7 . 1 Hector Mine , California , Earthquake as Inferred  
794 from InSAR and GPS Observations. *Bulletin of Seismological Society of*  
795 *America*, *92*, 1390–1402.

- 796 Sudhaus, H., & Jonsson, S. (2009). Improved source modelling through  
797 combined use of InSAR and GPS under consideration of correlated data  
798 errors : application to the June 2000 Kleifarvatn earthquake, Iceland. *Geo-*  
799 *physical Journal International*, 176, 389–404. doi:10.1111/j.1365-246X.  
800 2008.03989.x.
- 801 Sudhaus, H., & Jonsson, S. (2011). Source model for the 1997 Zirkuh earth-  
802 quake (Mw=7.2) in Iran derived from JERS and ERS InSAR observa-  
803 tions. *Geophysical Journal International*, 185, 676–692. doi:10.1111/j.  
804 1365-246X.2011.04973.x.
- 805 Thatcher, W., & Bonilla, M. G. (1989). Earthquake fault slip estimation from  
806 geologic, geodetic, and seismologic observations; implications for earth-  
807 quake mechanics and fault segmentation. *USGS Open-File Report*, 89,  
808 386–399.
- 809 Tse, S. T., & Rice, J. R. (1986). Crustal earthquake instability in relation  
810 to the depth variation of frictional slip properties. *Journal of Geophysical*  
811 *Research: Solid Earth*, 91, 9452–9472.
- 812 Wang, D., Chen, Y., Wang, Q., & Mori, J. (2018). Complex rupture of the  
813 13 november 2016 mw 7.8 kaikoura, new zealand earthquake: Comparison  
814 of high-frequency and low-frequency observations. *Tectonophysics*, 733,  
815 100–107.
- 816 Wang, R., Martin, F. L., & Roth, F. (2003). Computation of deformation  
817 induced by earthquakes in a multi-layered elastic crust—fortran programs  
818 edgrn/edcmp. *Computers & Geosciences*, 29, 195–207.

- 819 Wei, S., Fielding, E., Leprince, S., Sladen, A., Avouac, J.-P., Helmberger, D.,  
820 Hauksson, E., Chu, R., Simons, M., Hudnut, K., Herring, T., & Briggs, R.  
821 (2011). Superficial simplicity of the 2010 El Mayor-Cucapah earthquake  
822 of Baja California in Mexico. *Nature Geoscience*, *4*, 615–618. URL: <http://dx.doi.org/10.1038/ngeo1213>. doi:10.1038/ngeo1213.  
823
- 824 Williams, C. A., & Wallace, L. M. (2015). Effects of material property  
825 variations on slip estimates for subduction interface slow-slip events. *Geo-*  
826 *physical Research Letters*, *42*, 1113–1121.
- 827 Williams, C. A., & Wallace, L. M. (2018). The impact of realistic elastic  
828 properties on inversions of shallow subduction interface slow slip events  
829 using seafloor geodetic data. *Geophysical Research Letters*, *45*, 7462–7470.
- 830 Xu, X., Tong, X., Sandwell, D. T., Milliner, C. W. D., Dolan, J. F.,  
831 Hollingsworth, J., Leprince, S., & Ayoub, F. (2016). Refining the shal-  
832 low slip deficit. *Geophysical Journal International*, *204*, 1867–1886.  
833 doi:10.1093/gji/ggv563.
- 834 Zebker, H. A., Rosen, P. A., & Hensley, S. (1997). Atmospheric effects  
835 in interferometric synthetic aperture radar surface deformation and topo-  
836 graphic maps. *Journal of geophysical research: solid earth*, *102*, 7547–7563.
- 837 Ziv, A. (2016). Reconditioning fault slip inversions via insar data discretiza-  
838 tion. *Journal of Seismology*, *20*, 1123–1129.